Science Advances
AAAS

advances.sciencemag.org/cgi/content/full/5/4/eaav7662/DC1

Supplementary Materials for

Water vapor capturing using an array of traveling liquid beads for desalination and water treatment

A. Sadeghpour, Z. Zeng, H. Ji, N. Dehdari Ebrahimi, A. L. Bertozzi, Y. S. Ju*

*Corresponding author. Email: sungtaek.ju@ucla.edu

Published 12 April 2019, *Sci. Adv.* **5**, eaav7662 (2019)
DOI: 10.1126/sciadv.aav7662

This PDF file includes:

Supplementary Materials

Section S1. Full Navier-Stokes numerical simulation

We perform numerical simulation by solving the 2D axi-symmetric full Navier-Stokes equations for a flow of water along a string with average roughness of λ = 0.04 mm. Figure S2 shows the simulation domain and boundary conditions used. We implement the volume of fluid (VOF) method to track the water-air interface. We employ an unsteady 2D solver with the pressure staggering option (PRESTO) to handle the pressure-velocity coupling. A second-order upwind scheme is used to discretize the momentum equation. A quadratic mesh with the average element size of 0.015 mm and the number of mesh elements of approximately 400,000 is used in typical simulation runs.

Section S2. Mass transfer conductance of water substrate

We use the boundary layer theory for a flat surface to estimate the average mass transfer conductance over a liquid substrate, which is modeled as a cylinder.

Under our experimental conditions, the blowing factor, B_m *(28)*

$$B_m = \frac{m_{1,e} - m_{1,s}}{m_{1,s} - 1} \tag{1}$$

is estimated to be small, -0.07 < B_m < 0 and the zero normal velocity condition may be assumed to hold at the water-air surface. Using the established boundary layer theory for a flat surface, we obtain

$$\bar{g}_{m,sub} = \int_{0^+}^{L_{sub}} 0.332 \rho_m V_{air} \, \mathrm{Re}_x^{-1/2} \, Sc^{-2/3} dx \Big/ L_{sub} \tag{2}$$

The local Reynolds number is defined as $Re_x = \rho_m V_{air} \, x / \mu$, where the local coordinate x is shown in **Fig. 4A**. We use the analytic correlation for the boundary layer over a flat plate as a convenient and yet approximate expression for $\bar{g}_{m,sub}$ to quantitatively interpret our experimental data. To assess the accuracy of this approximation, we compare the average shear stress over the liquid substrate obtained using numerical simulation with that obtained using the analytic correlation. The estimated errors are approximately 4% for $\dot{m}_{Lps}$ =0.115 g/s and approximately 15% for $\dot{m}_{Lps}$ =0.035 g/s.

Section S3. Air side pressure drop model

The pressure drop consists of three major components: the frictional pressure drop dP_f, the pressure drop due to gravity dP_g and the pressure drop due to the momentum change dP_m

$$\frac{dP}{dz}=\left(\frac{dP}{dz}\right)_f+\left(\frac{dP}{dz}\right)_g+\left(\frac{dP}{dz}\right)_m \tag{3}$$

The pressure drop due to gravity $dP_g = \rho_m g dz$ in our setup is less than 7 Pa. The term dP_m results from vapor condensation and deceleration in the air stream *(34)*

$$\left(\frac{dP}{dz}\right)_m=\left(\frac{\dot{m}}{A_c}\right)^2\left(\frac{1}{\rho_m}+\frac{1}{\rho_w}\right)\frac{d\omega}{dz} \tag{4}$$

A_c represents the cross-section area for the air stream, ρ_w is the density of water, and ω is the humidity ratio.

The frictional pressure drop is the sum of the frictional pressure drops caused by liquid beads (sphere of diameter D_{bead} and the relative velocity of $V_{bead} + V_{air}$) and that by the liquid substrate (cylinder of diameter, D_{sub} and and the air stream velocity of V_{air}). The friction on the tube wall is estimated to be below 0.2 Pa, with the maximum corresponding to the air velocity of 0.75 m/s.

The frictional pressure drop for laminar flows along an array rod bundles *(30)* was given in terms of the friction factor f_L

$$f_L\,\mathrm{Re}\left(\frac{D_f}{D_h}\right)=\frac{8\sigma^2}{2(1-\sigma)-\ln(1-\sigma)-0.5(1-\sigma)^2-1.5} \tag{5}$$

$$\left(\frac{dP}{dz}\right)_f=\frac{2f_L\rho_m V_{air}}{D_h} \tag{6}$$

Here, $Re=\rho_m V D_h/\mu$ and V and μ are the relative air stream velocity and viscosity, respectively. D_h and D_f are the hydraulic diameter and the average liquid film diameter calculated from Nusselt solution, respectively *(23)*. The parameter σ represents the fraction of the total cross section available to the air flow.

Section S4. Effectiveness, heat flux, and overall performance comparison

In this section, we define and calculate the effectiveness of the dehumidifier. In a heat and mass exchanger, the modified heat capacity ratio, HCR, is defined as *(7, 38)*

$$HCR = \frac{\Delta \dot{H}_{\max,c}}{\Delta \dot{H}_{\max,h}} \tag{7}$$

HCR is the comparison between the maximum rate of change in the total enthalpy of the cold stream and that of the hot stream. The maximum rates of change can be obtained by assuming respective ideal conditions. In other words, $\Delta \dot{H}_{\max,h}$ is obtained from a condition where the outlet temperature of the air reaches the inlet temperature of the water. Likewise, $\Delta \dot{H}_{\max,c}$ can be obtained from a condition where the outlet temperature of the water reaches the inlet temperature of the air.

An energy-based effectiveness, ε, can then be defined for the dehumidifier in the following form

$$\varepsilon = \frac{\Delta \dot{H}}{\Delta \dot{H}_{\max}} \tag{8}$$

Here, $\Delta \dot{H}_{\max}$ is the maximum possible rate of change of enthalpy, $\min(\Delta \dot{H}_{\max,h}, \Delta \dot{H}_{\max,c})$, and the $\Delta \dot{H}$ is the actual rate change for one of the streams *(39)*.

Another performance parameter of dehumidifiers is the total heat exchanged between the coolant and the air-vapor mixture as discussed in Nayaran et al. *(14)*. Figure S6A and B show the effect of HCR on the energy-based effectiveness and the heat flux (kW/m^2), respectively. We can see that the effectiveness reaches the minimum when HCR is 1 (i.e. thermally balanced state). The same trend was reported by Nayaran et al. *(39)*. In contrast, the heat flux, $\dot{q}$, increases with increasing mass flow rates of either of the streams until it reaches a limit due to the limit on the rate of change in the total enthalpy of the other stream.

Table S1 shows the calculated values of ε and $\dot{q}$ for the present device and the existing technologies reported in the literature. All the dehumidifiers offer comparable effectiveness. We note that ε is a function of HCR (fig. S6A) and that a complete comparison is not feasible when ε was not reported over a wide range of HCR.

The heat flux, $\dot{q}$ [kW/m^2], is also provided for the different dehumidifiers in Table S1. One goal in designing a dehumidifier is to achieve the highest condensation rate in a unit volume, which is directly proportional to $\Delta \dot{H}$. The heat flux is related to the total enthalpy change through the following relation

$$\dot{q} = \frac{\Delta \dot{H}}{A_f} \tag{9}$$

where, A_f is the area for heat transfer from the hot air stream to the cold water stream in a given dehumidifier. Some dehumidifiers offer very high heat flux and yet poor overall performance due to their small heat transfer area. This deficiency can be captured by $\Delta \dot{H}$ or the overall capacity coefficient $g_m A_{int}/V_{deh}$.

The number of transfer units, N_{tu}, is defined as follows

$$N_{tu} = \frac{g_m A_{int}}{\dot{m}_w} \tag{10}$$

Here, $\dot{m}_w$ is the inlet mass flow rate of water. N_{tu} can be numerically calculated using *(28)*

$$N_{tu} = \int_{h_{w,in}}^{h_{w,out}} \frac{dh_w}{h_a - h_s} \tag{11}$$

where, h_a and h_w are the enthalpy of the saturated air (at T_{air}) and water (at T_{water}), respectively. h_s is defined as the enthalpy of saturated air at T_{water}. The values of h_w and h_s were obtained from existing literatures *(40)*. The enthalpy of the saturated air, h_a, is calculated using $h_a = h_{a,out} + \dot{m}_w / \dot{m}_a (h_w - h_{w,in})$. The overall capacity coefficient $g_m A_{int}/V_{deh}$, then, is calculated from N_{tu} using the following equation

$$\frac{g_m A_{int}}{V_{deh}} = \frac{N_{tu}\, \dot{m}_w}{V_{deh}} \tag{12}$$

Table S1 shows all the intermediate parameters used to calculate the overall capacity coefficients.

Table S1 lists the pressure drop, ε, $\dot{q}$, and overall capacity coefficient of our dehumidifier for a wide range of water-to-air mass flow rate ratio, $m_r = \dot{m}_{w,in} / \dot{m}_{a,in}$, (1.37 - 4.41), covering the range of m_r reported for the other dehumidifiers *(34-37)*.

The relative humidity, *RH*, measured at the air inlet and outlet of our dehumidifier is approximately 100% in all our experimental conditions. The mass of the condensed vapor can be calculated from the difference in water content of the inlet and outlet air streams. For our experimental cases the absolute condensation rate is in the range of 0.15-0.32 kg/h.

The ratio of the condensed water vapor to the total water vapor in the inlet air stream is calculated to be in the range of 0.31 to 0.85 for our dehumidifier. The smallest value, 0.31, corresponds to the 52-string configuration with the lowest water-to-air mass flow rate ratio (air superficial velocity of 0.7 m/s and water flow rate per string of 0.035 g/s). The highest value, 0.85, corresponds to the 96-string configuration with the highest water-to-air mass flow rate ratio (air superficial velocity of 0.23 m/s and water flow rate per string of 0.115 g/s).

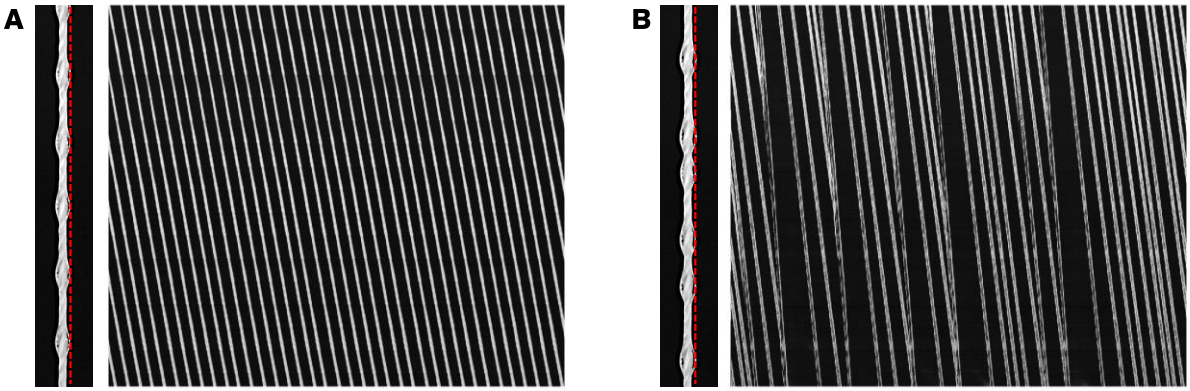

Fig. S1. Spatiotemporal diagram. The spatiotemporal diagram of a water film flowing down a cotton thread of diameter 0.76 mm and nozzle inner diameter of 1.2 mm. (**A**) The Rayleigh-Plateau regime where the trajectory lines are parallel, representing uniform bead spacing ($\dot{m}_{Lps}$ = 0.06 g/s) and (**B**) The convective instability regime where merging trajectory lines indicate coalescence ($\dot{m}_{Lps}$ = 0.14 g/s).

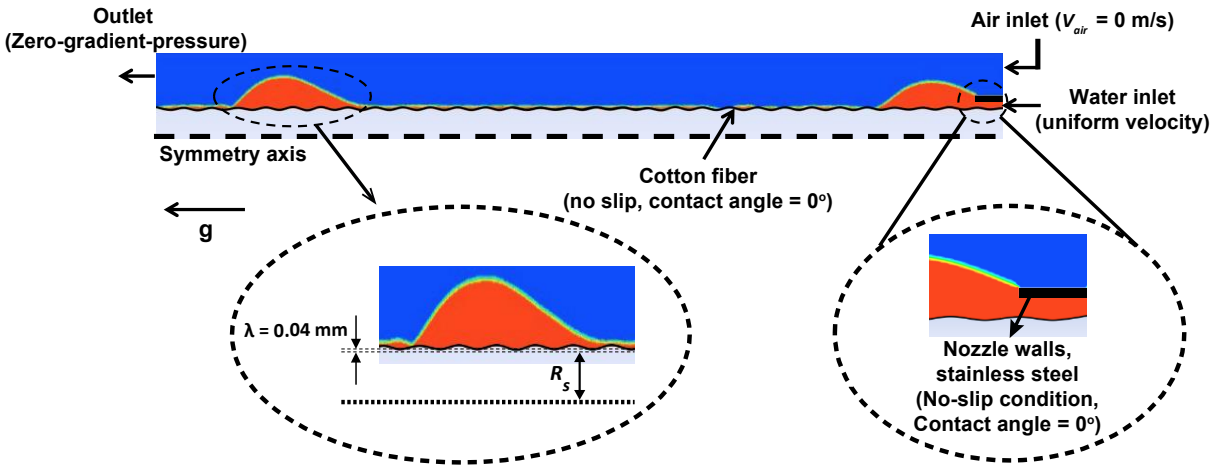

Fig. S2. Numerical simulation domain. Schematic of the simulation domain and the boundary conditions for the full 2D axi-symmetric Navier-Stokes simulations.

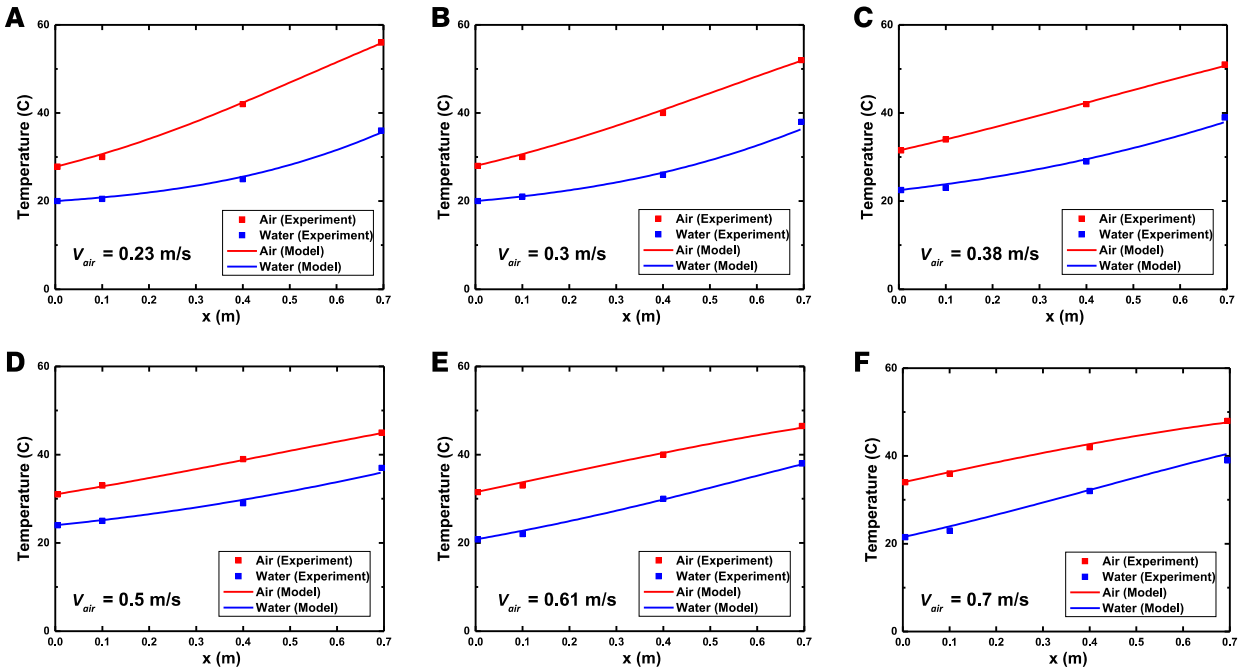

Fig. S3. Axial temperature profiles of the water and air streams. The experimental and model prediction results for the temperature profiles of the water and air streams along the dehumidifier (52 strings and $\dot{m}_{Lps}$ = 0.065 g/s) with the superficial air speed V_{air} of (**A**) 0.23 m/s, (**B**) 0.3 m/s, (**C**) 0.38 m/s, (**D**) 0.5 m/s, (**E**) 0.61 m/s, and (**F**) 0.7 m/s. The symbols represent the experimental results and the lines represent the model predictions.

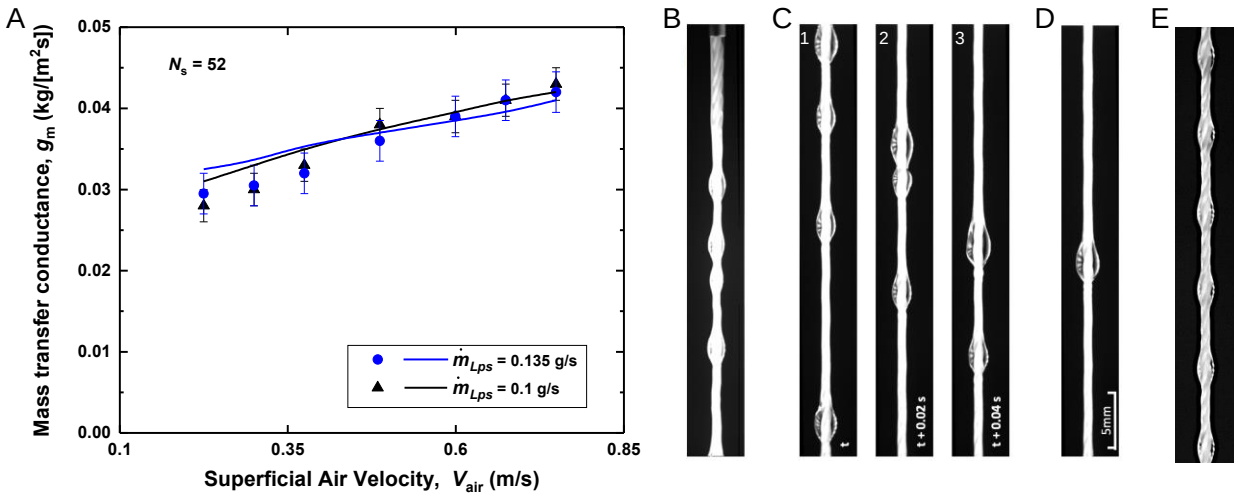

Fig. S4. The effect of the flow regimes on mass transfer. (**A**) The experimental and predicted mass transfer conductances as a function of the superficial air velocity. Two sets of data are shown, representing $\dot{m}_{Lps}$ = 0.1 g/s (RP regime) and $\dot{m}_{Lps}$ = 0.135 g/s (convective instability regime). The symbols represent the experimental results and the lines represent the model predictions. The error bars for the data for $\dot{m}_{Lps}$ = 0.135 g/s are bigger than those for the smaller water flow rate due to large variations in the geometric parameters of the beads in the convective instability regime. (**B-D**) The liquid film pattern at $\dot{m}_{Lps}$ = 0.135 g/s within 5 cm from the nozzle where the instability starts to disrupt the flat film region (**B**), within the next 5 cm region where

beads coalesce and form bigger beads (**C**), and in the semi-steady region where these bigger beads move at higher speeds (**D**). (**E**) The liquid film pattern with $\dot{m}_{Lps}$ = 0.1 g/s corresponds to the RP instability regime.

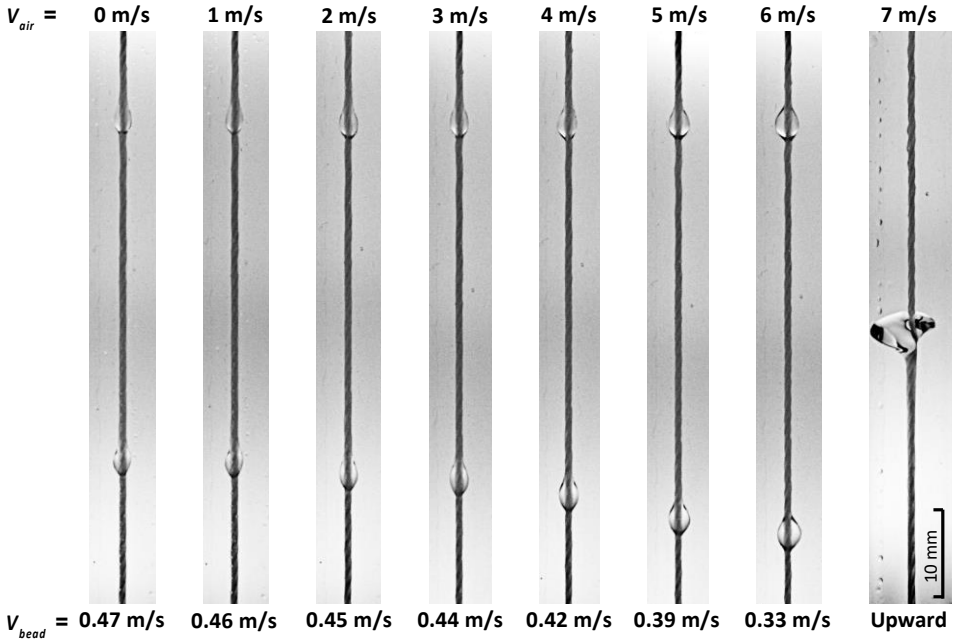

Fig. S5. Dynamics of water films flowing in countercurrent flows of air. The effect of counterflowing air streams on the dynamics of water film flows. Increasing air superficial velocities lead to increasing bead sizes and bead spacing. Only at very high air velocities (V_{air} > 7 m/s), well beyond the expected range used in dehumidifiers, water beads experience significant deformation and may reverse their directions.

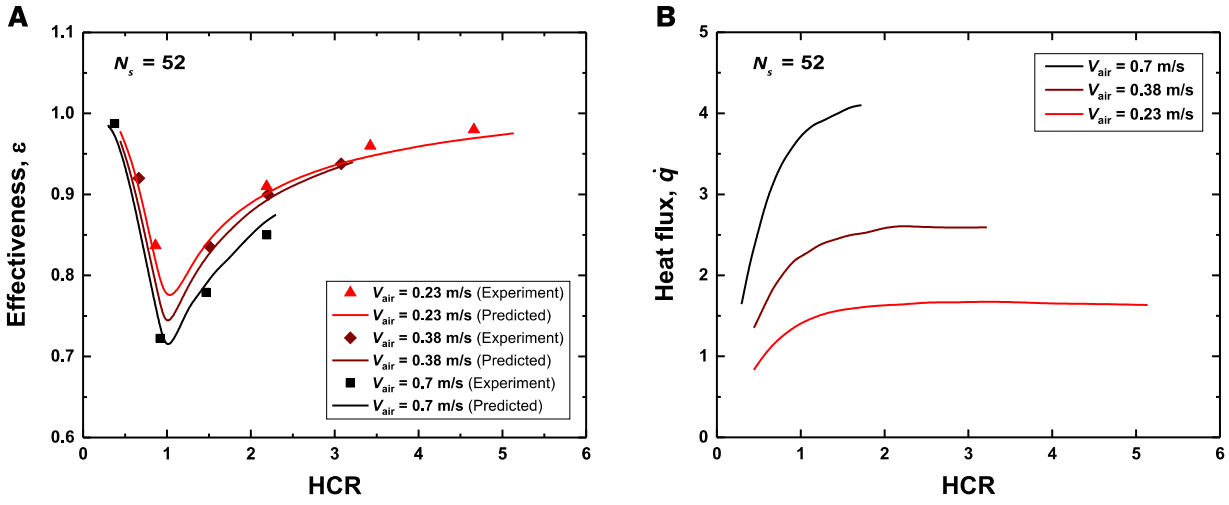

Fig. S6. Effectiveness and heat flux of dehumidifier. (**A**) Experimental results and model predictions of the energy-based effectiveness of dehumidifiers as a function of HCR for different superficial air velocities. (**B**) The effect of HCR on the heat flux for different superficial air velocities (model prediction results).

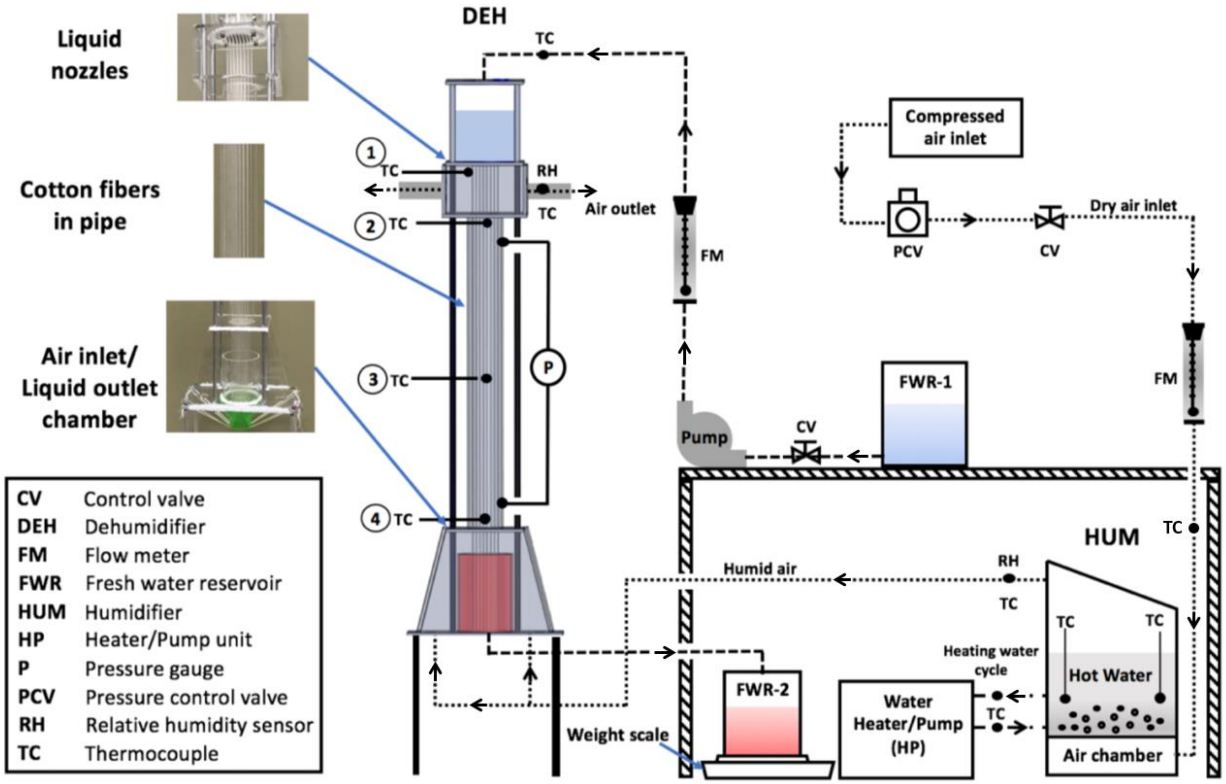

Fig. S7. Experimental setup. The schematic of the experimental setup used in this study.

Table S1. Dehumidifier comparison.

Dehumidifier	Our design				Plate & Tube	Flat Plate	Bubble Column	Shell& Tube
	N_s=96	N_s=96	N_s=96	N_s=52				
Air flow rate, $\dot{m}_a$ [g/s]	2.45	2.45	2.45	2.45	8.7	700	2	159
Water flow rate, $\dot{m}_w$ [g/s]	3.4	7	10.8	7	10.2	1300	8.3	227
Water/Air flow rate, m_r	1.37	2.85	4.41	2.85	1.17	1.86	4.17	1.42
Length, *L* (m)	0.7	0.7	0.7	0.7	1	1.9	0.04	0.6
Volume, V_{deh} (m^3)	0.00222				0.015	0.4844	0.0031	0.1991
Air inlet *T* [^{o}C]	49	49	48	41	59.5	60	70	58
Air outlet *T* [^{o}C]	30	24.5	23.8	25	48.5	42	49	48
Water inlet *T* [^{o}C]	21	21	22	20	25	15	20	30
Water outlet *T* [^{o}C]	44	33.5	30	27	58	46	43	56
NTU	2.07	1.11	0.76	0.71	1.19	0.60	0.30	1.01
g_m*A [g/s]	6.9	7.8	9.9	4.9	12.0	790	4.0	229.6
g_m*A/V [kg/s.m^3]	3.1	3.5	4.5	2.2	0.8	1.6	1.3	1.2
Pressure drop, Δ*P* [Pa]	9	9	9	8	25	32	400	18
Δ*P*/Length [Pa/m]	13	13	13	11	25	16.6	10000	29.6
Effectiveness, ε	0.9	0.91	0.94	0.85	0.94	0.85	0.86	0.9
Heat Flux, $\dot{q}$ [kW/m^2]	1.4	1.9	2.1	1.8	0.2-0.4	3.7	15	-